journal

Spatially Resolved Raman Spectroscopy Study of Transformed Zones in Magnesia-Partially-Stabilized Zirconia

Reinhold H. Dauskardt,*·* D. Kirk Veirs, and Robert O. Ritchie*

Center for Advanced Materials, Materials and Chemical Sciences Division,
Lawrence Berkeley Laboratory, University of California, Berkeley, California 94720

Raman vibrational spectroscopy provides an effective phase characterization technique in materials systems containing particle dispersions of the tetragonal and monoclinic polymorphs of zirconia, each of which yields a unique Raman spectrum. An investigation is reported to assess a novel, spatially resolved Raman spectroscopy system in the study of transformed zones surrounding cracks in partially stabilized MgO–ZrO$_2$ (PSZ). The experimental arrangement uses an imaging (two-dimensional) photomultiplier tube to produce a one-dimensional Raman profile of phase compositions along a slitlike laser beam without translation of either the sample or the laser beam and without scanning the spectrometer. For the present optical configuration, the spatial resolution is estimated to be equivalent to the detector resolution of 28 μm and does not appear to be reduced because of secondary scattering events in the PSZ. Results from phase characterization studies of the size, frontal morphology, and extent of transformation of transformation zones surrounding cracks produced under monotonic and cyclic loading conditions are presented. Particularly large zones are observed in the peak-toughened material, extending 1300 μm ahead of the crack tip with widths of up to 3000 μm. Good agreement is found with similar results determined using optical interference microscopy. [Key words: zirconia, magnesia, Raman spectroscopy, phase transformations, polymorphs.]

I. Introduction

MOST materials exhibit zones of nonlinear, elastically deformed material that surround cracks and which vary in geometric form with the local stress field developed near the crack tip. Examples of such zones are crack-tip plastic zones in metals, "crazed" zones in polymers, and transformation zones in metals and ceramics prone to stress-induced phase transformation. Depending on the prevailing mechanism of deformation, the presence of the zone can result in a marked reduction of the stress field near the crack tip, thereby effectively shielding the crack from the full applied stress. Although enhancement of the plastic-zone size has long been known to cause toughening in metals,[1] such "zone shielding" by crazing, microcracking, and transformation has more recently been shown to provide a potent toughening mechanism in polymers[2] and brittle ceramic materials.[3]

One quantitative description of such shielding has been obtained for ceramic systems containing a dispersion of metastable zirconia particles which martensitically transform from a tetragonal to a monoclinic crystal structure in the high stress fields

ahead of an advancing crack tip.[3–8] Several theoretical approaches, based on residual stress[4] or thermodynamic concepts,[5–8] have been advanced to account for the toughening achieved from principally dilatant transformation strains; in general, such approaches show consistent results.

Common to these approaches is the need to specify the transformation-zone shape. Although early theories considered only the hydrostatic component of the crack-tip stress field,[4,5] later studies have incorporated shear effects.[8–10] Depending on the selected transformation criterion, marked differences in the predicted shape of the frontal transformation zone may result. Because the attendant toughening not only scales with the zone width but is also modified by the frontal-zone shape, extent of transformation in the zone, and degree of reversibility of the transformation, precise specification of these zone parameters is important to facilitate a more complete theoretical understanding.

Detailed experimental studies of the transformation zone in zirconia-toughened ceramics have posed a particular challenge to material characterization techniques. In fact, the decreasing degree of transformation of zirconia particles from the crack plane (as opposed to a step-function discontinuity where all particles within a well-defined boundary transform) has only very recently been verified[11] by measuring the surface uplift surrounding the crack using optical-interference microscopy and calculating the distribution of transformation strains in the zone as a function of the resulting surface displacements. Few other characterization techniques are presently available. For example, although ideal for particle-phase, orientation, and nucleation studies, transmission and scanning transmission electron microscopy techniques are essentially limited by their small analysis volumes and time-consuming specimen-preparation requirements,[12–14] and can lead to microstructural aberrations associated with thin-foil preparation and spontaneous transformation under the electron beam. Conversely, techniques such as X-ray diffraction (XRD) and channeling-pattern analysis in scanning electron microscopy typically do not have sufficient resolution to distinguish microstructural variations in the zones. However, XRD in the form of texture analysis can be useful in the determination of a crystallographic bias of the transformation variants.[15]

The observation of transformation zones with optical microscopy, specifically using Nomarski interference, can furnish a rapid and convenient preliminary means of characterization, particularly of zone morphology, but further quantitative information is limited.[16–18] Analysis of the fringe pattern obtained from interference microscopy to determine the surface uplift associated with the transformation zone may similarly be used to provide a more sensitive indication of the extent of the zone.[11] Calculation of the degree of transformation, however, requires a relatively laborious analysis of the fringe pattern. More detailed characterization can be achieved with Raman microprobe analysis,[19–22] where the distinct and strong characteristic Raman vibrational spectra of the monoclinic and tetragonal polymorphs in zirconia provide a clear means of identification.[23–25] Phase analysis in the transformed zone is achieved by scanning a small ($\approx$1-μm diameter) Raman microprobe across the zone; volume fractions are deduced

from a calibrated function of the strengths of the respective phase-characteristic peaks in the Raman signal.

The objective of the present study was to evaluate the capabilities of a novel, spatially resolved Raman spectroscopy system[26] for the characterization of phase transformation in partially stabilized zirconia (PSZ). This system, having a unique combination of high sensitivity, low noise, and multiplexed spatial resolution, was used to image and characterize 256 contiguous volumes of material forming a thin, bandlike analysis region positioned over an area of interest. The multiplexed capability of the system allows analysis of the contiguous volumes to be achieved simultaneously. Successive translations of the specimen therefore allow a composite two-dimensional map of the phase distribution over an area of interest to be determined. Specifically, the study was intended to provide a detailed phase characterization of the transformation-zone size and morphology surrounding monotonically and cyclically loaded cracks.

Fig. 1. Schematic of beam-shaping and collecting optics for spatially resolved Raman spectroscopy.

II. Material

Zirconia, partially stabilized by the addition of 9 mol% MgO and heat-treated to exhibit varying degrees of transformation toughening (MgO–PSZ), was selected for the present study. The microstructure of this material consists of cubic ZrO_2 grains, 50 μm in diameter, containing lens-shaped tetragonal precipitates ($\approx$35 to 40 vol%) with maximum dimension of 300 nm.[16] Extensive microstructural and mechanical-property characterization is described elsewhere.[6,16,18,27-29]

MgO–PSZ displays marked resistance-curve (R-curve) behavior where the toughness increases with crack extension, characteristic of significant crack-tip shielding. In the "peak-toughness" condition, fracture toughnesses of $\approx$3.9 MPa·m$^{1/2}$ were measured at crack initiation (K_i) and $\approx$18 MPa·m$^{1/2}$ at the steady-state plateau of the R-curve (K_c). In addition, a "low-toughness" condition, with $K_c \approx 5.5$ MPa·m$^{1/2}$, and a reference "overaged" condition, with $K_c \approx 3.9$ MPa·m$^{1/2}$ (where all tetragonal particles were transformed to the monoclinic phase), were obtained using appropriate "aging" treatments.

Cracks, with their associated transformation zones, were produced under well-defined monotonic- or cyclic-loading conditions in 3-mm-thick compact tension specimens, tested in controlled room-temperature air using automated electro-servo-hydraulic testing machines. Comprehensive experimental and crack-monitoring techniques required to produce long (>3 mm) through-thickness cracks under monotonic- and fatigue-loading conditions in this material were reported previously.[29] Prior to crack growth, the surfaces of the specimens were polished to an optical finish, previously shown to contain at most $\approx$14% monoclinic content, of which a portion is due to the polishing operation.[16] To facilitate comparison, the transformed zones were also observed in the optical microscope using optical interference (including Nomarski) techniques.

An indication of the resolution and analysis volume of the spatially resolved Raman technique was determined through analysis of suitable sections containing sharp edges and known interfaces between samples of PSZ containing differing amounts of monoclinic phase. For example, an interface was prepared between PSZ in the peak-toughness and low-toughness conditions by bonding together two specimen edges. The maximum surface separation of the resulting interface due to nonuniform polishing was measured to be no greater than 30 μm.

III. Spatially Resolved Raman Spectroscopy

Zirconia has three well-defined crystalline polymorphs, with cubic, tetragonal, and monoclinic structures;[23-25] the latter two may be uniquely characterized by a distinct vibrational (or Raman) spectrum. Raman vibrational spectroscopy therefore provides an ideal phase-characterization technique in materials containing dispersions of these polymorphs.

In the present study, the experimental arrangement makes use of an imaging (two-dimensional) photomultiplier tube (PMT)
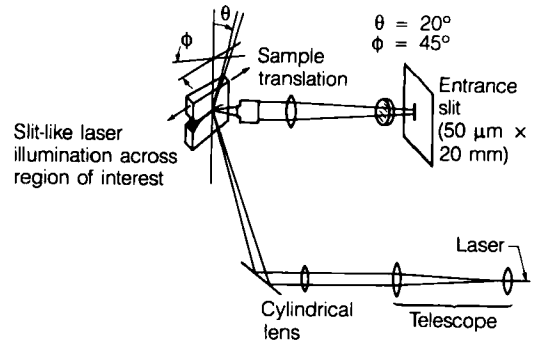
which is capable of producing a one-dimensional profile of the chemical composition along a laser beam using Raman spectroscopy, without translation of either the sample or the laser beam. The Ar$^+$ laser (2 mW at 488 nm) is focused on the PSZ sample using a combination of one cylindrical and two spherical lenses, as illustrated schematically in Fig. 1. The laser is incident at 70° from the surface normal and forms a slitlike illumination, 25 μm wide by 3 mm high. Scattered light is collected and focused using a 50-mm $f/1$ camera lens onto the 48-μm-wide entrance slit of the spectrometer. The image of the slitlike illuminating laser beam is aligned onto the entrance slit by adjusting the rotation of the cylindrical lens. The size of the slitlike analysis area may therefore be varied readily by adjustment of both the beam shaping and collecting optics. For high-resolution imaging, the camera lens can be replaced with a microscope objective lens. A six-cavity interference filter is used to reject the Rayleigh line by >10^4. The bandwidth of the interference filter encompasses the 100- to 500-cm^{-1} range of interest for zirconia polymorphs.

At the detector, the spectrometer optics form an image of the scattered light with position along the entrance slit resolved in the vertical direction and wavelength disperison resolved in the horizontal direction. Thus, each vertical position at the detector contains the Raman spectrum of a corresponding volume of material in the slitlike analysis region. By using a two-dimensional detector, such as an imaging PMT, the Raman spectrum of each contiguous volume of material is observed without translating the sample or scanning the spectrometer. In this study, the Raman image contains 256 elements (linear pixel arrays) along the laser beam; the total collection time is typically 7.5 min. Real-time cathode-ray tube display of each detected photon assists in sample alignment. In addition, these data are stored in memory accessible to a microcomputer and may be manipulated and analyzed to facilitate graphic display of relative intensity, and the spatial variation of the composition. More detailed explanations of the experimental arrangement and automated data processing were reported previously.[26]

IV. Theory

The intensity of Raman scattered light from some finite volume containing a multiphase material is given by

$$I = I_y \sum_i \left(N_i \sum_{j=1}^{x_i} (\partial\sigma_j/\partial\Omega)_i \right) \qquad (1)$$

where I_y is the intensity of the incident light, N_i the density of scatters within the volume of interest with chemical composition and phase i, X_i the number of allowed Raman vibrations of phase i, and $(\partial\sigma_j/\partial\Omega)_i$ the Raman cross section of the jth Raman-allowed vibration of phase i. The Raman cross section of the jth allowed vibration of phase i can be expressed as a function of energy.
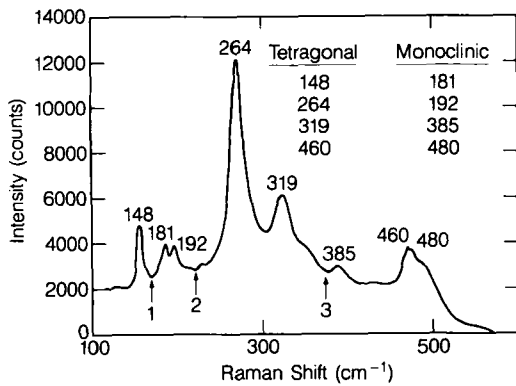
Fig. 2. Characteristic Raman spectrum of MgO–PSZ ceramic containing monoclinic and tetragonal precipitates. The peaks at 181, 192, 385, and 480 cm^{-1} are characteristic of the monoclinic phase and the peaks at 148, 264, 319, and 460 cm^{-1} of the tetragonal phase.

$$(\partial\sigma_j/\partial\Omega)_i = C(\nu_l - \nu_{ji})^4 \alpha_{ji}^2 g_{ji}(\nu) \qquad (2)$$

where C is a collection of constants, ν_l the energy of the incident light (in cm^{-1}), ν_{ji} the vibrational energy (in cm^{-1}), α_{ji} the polarizability matrix element for the jth transition in phase i, and $g_{ji}(\nu)$ the lineshape function. The lineshape function, centered at ν_{ji}, satisfies $\int g_{ij}(\nu)\,d\nu = 1$. In a Raman experiment, the observed spectrum is also influenced by the wavelength-dependent instrument response, $R(\nu)$, and by a background due to fluorescence, stray light, and other sources. The background can be determined and subtracted from the observed spectrum, as discussed in the following section. Combining Eqs. (1) and (2) with $R(\nu)$ yields the observed background-corrected Raman spectrum

$$I(\nu) = I_y R(\nu) \sum_i \left\{ N_i \sum_{j=1}^{x_i} [C(\nu_l - \nu_{ji})^4 \alpha_{ji}^2 g_{ji}(\nu)] \right\} \qquad (3)$$

The relative amounts of the components i contributing to the observed spectrum can be determined in a number of ways. If all the components are known (i.e., central energies, lineshapes, and polarizability matrix elements) with the instrumental response function, then the spectrum can be fitted by varying N_i with potentially extremely accurate results; in practice this method is difficult. In many cases there are strong characteristic Raman transitions for each component which are well separated in energy from all other observed Raman transitions. Such transitions can be used for mole-fraction determinations by using either their maximum or their integrated intensities. Using the integrated intensity typically yields a determination with less error because of counting statistics and is readily implemented with computerized data acquisition.

The estimated signal, S_{nm}, from an allowed Raman transition n of component m, is obtained by integrating Eq. (3) over a small energy range, 2δ, centered at ν_{nm} in which $g_{ji}(\nu) \approx 0$ for all other components.

$$S_{nm} = \int_{\nu_{ji}-\delta}^{\nu_{ji}+\delta} I(\nu) = I_y \overline{R} N_m C(\nu_l - \nu_{nm})^4 \alpha_{nm}^2 \qquad (4)$$

where $\overline{R}$ is the average value of $R(\nu)$ over the range of integration. In a system containing two phases of interest such as PSZ, the integrated intensities for isolated peaks due to the monoclinic phase, S_{mono}, compared with those of the tetragonal phase, S_{tet}, may be expressed as the ratio

$$\frac{S_{mono}}{S_{tet}} = \kappa \frac{N_{mono}}{N_{tet}} \qquad (5)$$

where

$$\kappa = \frac{\overline{R}_{mono}(\nu_l - \nu_{mono})^4 \alpha_{mono}^2}{\overline{R}_{tet}(\nu_l - \nu_{tet})^4 \alpha_{tet}^2} \qquad (6)$$

This ratio is independent of the incident light and depends on the relative concentration of the monoclinic phase to the tetragonal phase in the volume sampled. The value of κ can be determined from a sample with known composition or from the slope of the signal ratio from a series of samples with known but varied compositions.

V. Data Analysis

A representative Raman spectrum of the polished surface of the peak-toughened PSZ is presented in Fig. 2. The characteristic vibrational energies of the monoclinic and tetragonal phases are indicated.[19,23-25] The typically strong 460 and 480 cm^{-1} peaks appear significantly weaker than the 264 cm^{-1} peak because of the interference-filter cutoff; the red-edge interference filter cutoff in the transmission is readily apparent at 500 cm^{-1}. The significant background throughout the spectrum is caused by scattering of light within the spectrometer and processes at the sample such as fluorescence and phonon scattering.

The estimated signal of the monoclinic phase, S_{mono}, was arbitrarily defined as the integrated intensity of the 181 and 192 cm^{-1} line pair, determined by summing over 30 pixels centered at 186 cm^{-1} and subtracting 30 times an average background for that region. Background signals (counts/pixel) were determined at the points in the spectrum marked *1*, *2*, and *3*. The average background for the monoclinic peak was determined from the background signals at points *1* and *2*. The estimated signal of the tetragonal phase, S_{tet}, was arbitrarily defined as the integrated intensity of the 264 cm^{-1} peak,[†] determined by summing over 40 pixels centered at 264 cm^{-1} and subtracting 40 times an average background from the average intensity at points *2* and *3*. The noise in the spectrum is statistical and directly proportional to the square root of the number of counts. To ensure that the signal of the monoclinic or tetragonal phase was real and nonzero, the following criterion was employed: if S_{mono} (or S_{tet}) was less than 3 times the square root of the background, then S_{mono} (or S_{tet}) was set at zero.

The relative fraction of the monoclinic phase, F_{mono}, compared with the total monoclinic plus tetragonal phase, is defined as

$$F_{mono} = \left(\frac{N_{mono}}{N_{mono} + N_{tet}}\right) \times 100\%$$

$$= \left(\frac{S_{mono}}{S_{mono} + \kappa S_{tet}}\right) \times 100\% \qquad (7)$$

where the value of κ was set to 1.0. Previous studies suggest that this is not an unreasonable estimate.[19] Note that small changes in the value of κ result in correspondingly small changes in the magnitude of F_{mono}. Changes in the observed spatial distribution of the monoclinic phase, as obtained by variations in F_{mono}, however, remain unaffected.

The calculated percentage is dependent only on the number densities and not on other experimental parameters such as the illuminating-light intensity or light-collection efficiency. The error in F_{mono} is, however, dependent on the incident light intensity and increases as I_y decreases because of increased relative uncertainties arising from fewer observed counts. Increased noise, leading eventually to uncertain data, may therefore be expected at the edges of the detector exposed to low-intensity light arising from the tail ends of the Gaussian intensity distribution at the extremes of the entrance slit. Potential improvements to the technique should therefore include modifying the laser-beam shaping optics to achieve a more uniform slitlike illumination at the sample.

[†]The relatively small 148-cm^{-1} peak, lying both on the edge of the active area of the detector, where distortions occur, and on the blue edge of the interference filter cutoff, was not used in determining the tetragonal signal intensity as has been reported previously,[19] because it contributes only a marginal fraction compared with the 264-cm^{-1} peak intensity.
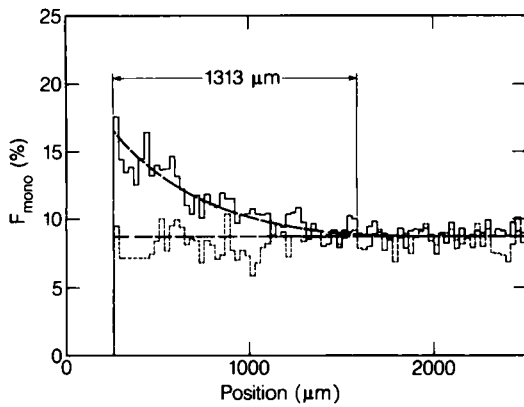
Fig. 3. Raman profile of the relative fraction of monoclinic phase (F_{mono}), as a function of distance from the edge of a through-thickness crack. A similar profile of F_{mono}, adjacent a sharp edge containing no transformation zone, is included for comparison.
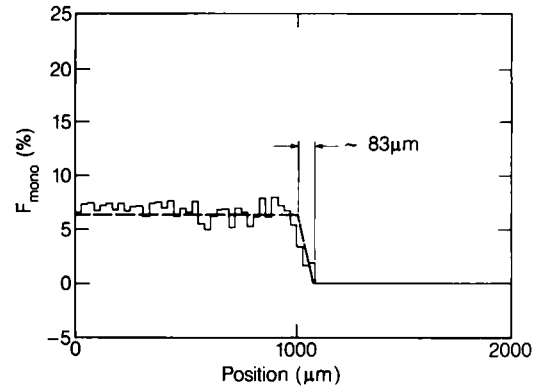

Fig. 4. Representative Raman profile of the relative fraction of monoclinic phase (F_{mono}) as a function of distance across a known peak-toughness/low-toughness interface.

VI. Results

(1) Resolution

The relative fraction of the monoclinic phase, F_{mono}, as a function of distance from the edge of a through-thickness crack in peak-toughened PSZ, is shown in Fig. 3. A similar Raman profile of the monoclinic fraction adjacent a sharp edge containing no transformation zone is included for comparison. The edge of the crack face and specimen appear as abrupt increases in F_{mono} from 0% to 20% and 9%, respectively. F_{mono} then remains constant in the specimen adjacent the sharp edge and decreases smoothly to the bulk value of 9% in the transformation zone adjacent the crack face. The extent of the transformation zone of approximately 1313 μm is similar to that determined by Nomarski interference of the same region.

F_{mono}, as a function of distance across the peak-toughness/low-toughness interface, was observed at four locations along the interface. A representative profile is shown in Fig. 4; the transition region, from 7% F_{mono} of the peak-toughened region to 0% F_{mono} of the low-toughness toughened region, occurs over approximately 83 μm.

transformation behind the crack tip. The spatial extent of the zone shows good agreement with that observed using Nomarski interference, as illustrated in Fig. 8. Note that, because of the

(2) Transformation Zones

(A) Monotonic Loading: The relative fraction of the monoclinic phase, F_{mono}, as a function of distance perpendicular to the plane of a through-thickness crack in the peak-toughened material, was obtained at two locations along the crack path, and seven ahead of the crack tip. The profiles were separated by 254 μm. A typical profile located $\approx$508 μm behind the tip of the crack is presented in Fig. 5. The crack had arrested naturally after growing unstable under monotonic loading. A similar profile at a distance of $\approx$762 μm ahead of the crack tip is included for comparison. A further indication of the extent of the frontal zone was determined from a profile centered and parallel to the plane of the crack, extending ahead of the crack tip (Fig. 6). To present a two-dimensional view of the transformation zone, the data from the above profiles were replotted as a contour map (Fig. 7). The extent of, and degree of transformation in, the zone is immediately apparent from this representation. In addition, the marginal decrease in both the size of the transformation zone and the de-
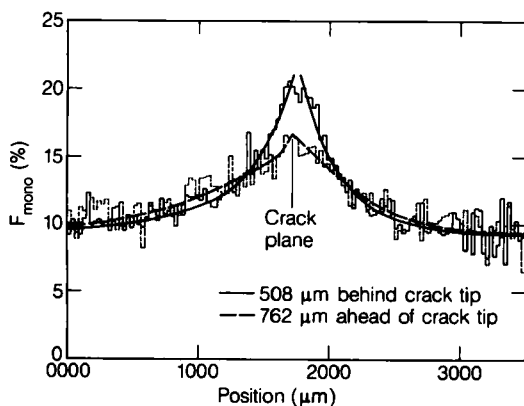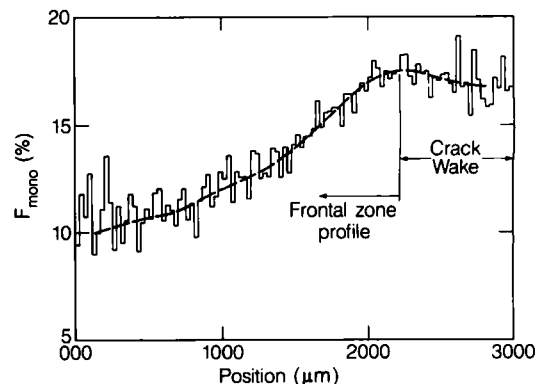

Fig. 5. Raman profile of the relative fraction of monoclinic phase (F_{mono}) as a function of distance across a through-thickness crack, at positions located $\approx$508 μm behind and $\approx$762 μm ahead of the crack tip.

Fig. 6. Raman profile of the relative fraction of monoclinic phase (F_{mono}) as a function of distance ahead of a through-thickness crack.

gree of transformation was observed behind the crack tip. It is not apparent from these preliminary studies whether this represents a surface aberration or is an indication of reversibility of the gradual decrease in the degree of transformation toward the edges of the transformation zone, the maximum extent of the zone as revealed by variation of the contrast using Nomarski interference is difficult to determine.

(B) Cyclic Loading: The transformation zone surrounding a crack produced under tension–tension cyclic-fatigue loading conditions was also evaluated. Variation of the applied stress-intensity range along the crack path, from $\Delta K = 7.9$ to 10.7 MPa·$m^{1/2}$, resulted in fatigue-crack propagation rates (da/dN) ranging from 3.0×10^{-11} to 3.0×10^{-6} m/cycle. The crack was subsequently loaded monotonically until final fracture to determine the R curve. The resulting fracture profile is apparent in the interference micrograph shown in Fig. 9(A). Successive fringes in the pattern indicate contours of elevation on the tilted specimen surface. The surface displacements in the transformation zone cause the fringes to deviate from linearity, producing the curved geometry. Detailed analysis of the fringe pattern may be undertaken to reveal the degree of transformation in the zone.[11] In the present study, however, only the point of first deviation from linearity of the fringes was determined in order to provide some indication of the zone width. The results of this analysis are presented in Fig. 9(B).

Raman profiles of the relative monoclinic fraction, F_{mono}, as a function of distance perpendicular to the plane of the crack, were obtained at positions *1* to *8*, as shown in Fig. 9(B). A typical profile taken at position *1* is presented in Fig. 10. The profiles were characterized by a marked decrease in degree of transformation over the first $\approx 30\%$ of the zone, followed by a more gradual decrease to the edge of the zone boundary. The maximum spatial extent of the zone, as indicated by an increase in F_{mono} above background, was determined and is presented in Table I, with similar results from the interference analysis. In addition, the extent of the transformation zone at $F_{mono} = 12\%$, which represents a zone containing at least 65% of the transformed precipitates, is included for comparison. An error of ± 150 μm (approximately 14% of the zone width) was estimated for the maximum extent of the zone, because of the gradual slope of the profile toward the

Table I. Comparison of Spatial Extent of the Transformation Zone Using Raman Spectroscopy and Interference Microscopy

| | Transformation-zone half-width (μm) | | |
| | Raman spectroscopy | | |
Position	$F_{mono} = 12\%$	$F_{mono} =$ background	Interference microscopy
1	798	2154	2394
2	566	2379	2508
3	450	2258	2394
4	435	2206	2223
5	334	2084	2166
6	319	2067	2109
7	406	2188	2223
8	464	1980	2138

zone boundary. A reduced error of ± 36 μm was observed at the $F_{mono} = 12\%$ boundary. The extent of the zone at the $F_{mono} = 12\%$ boundary was similar to that estimated from Nomarski interference of 400 μm. These results are consistent, considering the inherent difficulty of assessing subtle variations in contrast present at the outer extent of the zone using Nomarski interference.

VII. Discussion

MgO–PSZ is a translucent material which substantially scatters light. Raman-scattered light from one region therefore may be secondarily scattered into an adjacent region. Using a microprobe configuration, the axial spatial resolution of the analysis volume is determined by the depth of focus of the incident light and the depth of field of the collection optics.[30-32] Similarly, the lateral spatial resolution is also determined by characteristics of the illuminating and collecting lenses. The resolution of the analysis volume may therefore be optimized to the required degree by suitable lens and aperture configurations.[19,20,30-32]

Peculiar to multiplexed, spatially resolved Raman spectroscopy is the question of lateral spatial resolution at any point along the striplike analysis volume. An inherent limit on this resolution is naturally determined by that particular region of the analysis area imaged directly onto each position (linear pixel array) at the detector. For the present optical configuration, each pixel resolves 27.7 μm along the length of the striplike analysis volume. However, additional reduction in resolution due to secondary scattering may conceivably contribute to a substantial broadening of a sharp transition of composition along the analysis region. In addition, optical artifacts at regions near sharp edges and crack faces may also produce anomalous results. Examination of the Raman profile of the relative monoclinic fraction across a sharp edge (Fig. 3), however, indicates that edge effects do not appear. In this case the bulk relative fraction of monoclinic phase of 9% is seen immediately at the edge. In addition, the change in F_{mono} across a known sharp interface (Fig. 4), from 7% in the peak-toughened condition to 0% in the low-toughness condition, occurred over, at most, 83 μm. The interface itself had a surface opening of 30 μm due to microscopic roughness of the specimen
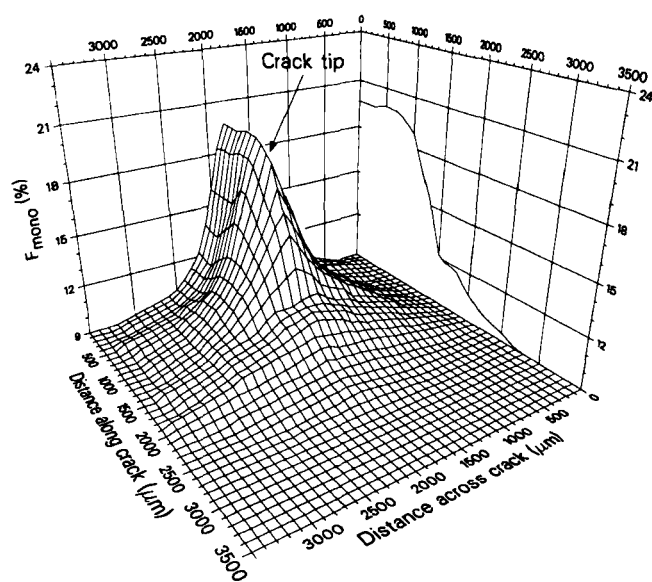

Fig. 7. Three-dimensional Raman plot of the morphology of the transformed zone both ahead and in the wake of the crack tip in peak-toughened MgO–PSZ. Contour map has spatial coordinates in the horizontal plane and degree of transformation in the vertical plane.
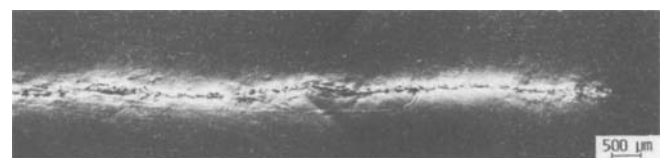

Fig. 8. Optical micrograph, using Nomarski interference contrast, indicating the extent of the transformation zone surrounding the through-thickness crack. Close agreement with the zone morphology, determined using Raman spectroscopy, is apparent by comparison with Fig. 7.
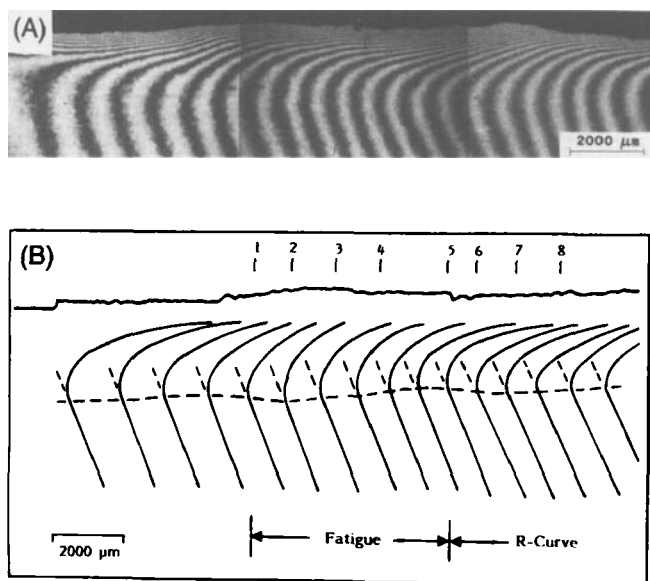
Fig. 9. Interference microscopy of the crack profile and transformation zone containing regions of cyclic fatigue and monotonic loading, showing (A) the interference micrograph and (B) interpretation of the fringe pattern.
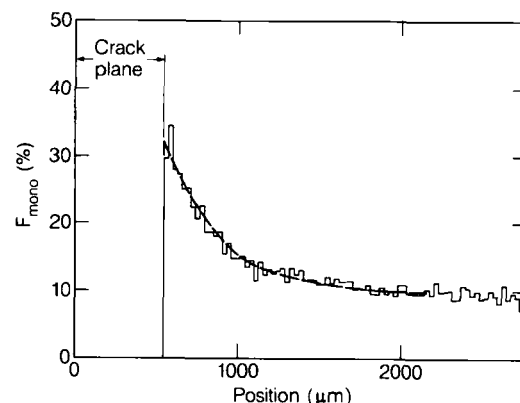

Fig. 10. Typical Raman profile of the relative fraction of monoclinic phase (F_{mono}) as a function of distance from the edge of the through-thickness crack. The profile was located at position I in Fig. 9(B).

edges. The observed transition, therefore, occurs over 28 μm (1 pixel) on either side of this gap and is taken to be the spatial resolution with the current optical arrangement.

The morphology of the crack-tip transformation zone observed in Fig. 6 appears to conform more to a critical hydrostatic-stress transformation criterion than to the fabiform shape expected for shear-assisted nucleation. It is possible, however, that the critical nucleation criterion might be sensitive to particular loading conditions and crack-propagation rates. Indeed, despite the strong athermal nature of the transformation, recent experimental evidence suggests that thermal activation may play a minor role.[15,33] Unstably propagating and highly stressed cracks may therefore be expected to exhibit deviant-zone morphologies as thermal activation is suppressed. In light of these possible contributions to the critical transformation criterion, interpretation of the transformation zone in Fig. 6, which resulted from the arrest of an unstably propagating crack, may be complicated. In addition, the zone observed at the specimen surface reflects a plane-stress condition, which may differ considerably from that formed in plane strain in the specimen interior.

Cyclic fatigue-crack propagation under tension–tension loading has recently been observed in toughened PSZ ceramics.[29] Observation of the spatial extent of the resulting transformation zone using both Raman (Fig. 10) and interference (Fig. 9) techniques, indicated consistently lower zone widths with the Raman measurements (Table I). A small region of elastic surface displacement surrounding the transformation zone, which would be reflected by an earlier deviation from linearity of the interference fringes but remain invisible in the Raman profile, may have contributed to this discrepancy. Qualitative confirmation for the initial rapid decrease in the degree of transformation in the zone, observed in the Raman profiles, was also apparent in the interference micrographs, which showed an acute increase in fringe density immediately adjacent the crack face in the transformation zone. More detailed studies of the mechanisms of cyclic fatigue-crack propagation in these materials are however, beyond the scope of the present study and will be presented elsewhere.[34]

VIII. Conclusion

An investigation designed to assess a novel Raman spectroscopy system for the study of phase-transformation zones in MgO–PSZ is reported. The Raman spectroscopy system, having a unique combination of high sensitivity, low noise, and multiplexed spatial resolution, is employed to simultaneously characterize 256 spatial elements 25 μm wide by 28 μm high, forming a thin slitlike band of material positioned over a region of interest. Spatial resolution, as determined by the ability to distinguish adjacent areas with different composition, is limited in the present configuration by the detector pixel size of 28 μm. Noninstrumental limitations, such as secondary scattering from adjacent areas in the sample, do not appear to have influenced the spatial resolution.

Transformation zone widths surrounding cracks in peak-toughened PSZ were measured to be 1000 to 1500 μm for a variety of fracture conditions. Successive translation of the specimen allows a quantitative two-dimensional Raman map of the phase distribution on the specimen surface to be determined rapidly. Detectable changes in the fraction of monoclinic phase occurred up to 1300 μm ahead of the crack tip.

The transformation zones were also characterized using interference microscopy and optical microscopy with Nomarski interference contrast. Close agreement is found between the extent of the transformation zones determined from interference microscopy and Raman techniques. Although appropriate for preliminary analysis, substantially smaller zone widths of approximately 400 μm, containing $\approx$65% of the transformed material, were observed using Nomarski interference microscopy.

References

[1]R. W. Hertzberg, Deformation and Fracture Mechanics of Engineering Materials, 2d. ed.; Ch. 8. Wiley, New York, 1983.

[2]A. S. Argon, R. E. Cohen, and O. S. Grbilioglk, "Mechanistic and Continuum Aspects of Toughness in Heterogeneous Polymers"; pp. 3–14 in Mechanical Behavior of Materials, Vol. 1. Edited by M. G. Yan, S. H. Zhang, and Z. M. Zheng. Pergamon Press, Oxford, UK, 1987.

[3]R. C. Garvie, R. H. Hannick, and R. T. Pascoe, "Ceramic Steel?," *Nature (London)*, 258 [5537] 703–704 (1975).

[4]R. M. McMeeking and A. G. Evans, "Mechanisms of Transformation Toughening in Brittle Materials," *J. Am. Ceram. Soc.*, 65 [5] 242–45 (1982).

[5]B. Budiansky, J. W. Hutchinson, and J. C. Lambropoulos, "Continuum Theory of Dilatant Transformation Toughening in Ceramics," *Int. J. Solids Struct.*, 19 [4] 337–55 (1983).

[6]A. G. Evans and R. M. Cannon, "Toughening of Brittle Solids by Martensitic Transformations," *Acta Metall.*, 34 [5] 761–800 (1986).

[7]D. B. Marshall, A. G. Evans, and M. Drory, "Transformation Toughening in Ceramics"; pp. 289–307 in Fracture Mechanics of Ceramics, Vol. 6. Edited by R. C. Bradt, A. G. Evans, D. P. H. Hasselman, and F. F. Lange. Plenum Press, New York, 1983.

[8]L. R. F. Rose, "The Mechanisms of Transformation Toughening," *Proc. R. Soc. London, Sect. A*, 412, 169–97 (1987).

[9]J. C. Lambropoulos, "Shear, Shape, and Orientation Effects in Transformation Toughening," *Int. J. Solids Struct.*, 22 [10] 1083–1106 (1986).

[10]I-W. Chen, "Implications of Transformation Plasticity in ZrO_2-Containing Ceramics: I, Shear and Dilatation Effects," *J. Am. Ceram. Soc.*, 69 [3] 181–89 (1986).

[11]B. N. Cox, D. B. Marshall, D. Kouris, and T. Mura, "Surface Displacement Analysis of the Transformed Zone in Magnesia-Partially-Stabilized Zirconia," *J. Eng. Mater. Technol.*, 110 [4] 105–109 (1988).

[12]D. L. Porter and A. H. Heuer, "Mechanisms of Toughening Partially Stabilized Zirconia (PSZ)," *J. Am. Ceram Soc.*, 60 [3–4] 183–84 (1977).

[13]H. Ruf and A. G. Evans, "Toughening by Monoclinic Zirconia," *J. Am. Ceram. Soc.*, 66 [5] 328–32 (1983).

[14]A. H. Heuer and M. Rühle, "On the Nucleation of the Martensitic Transformation in Zirconia (ZrO_2)," *Acta. Metall.*, 33 [12] 2101–12 (1985).

[15]I-W. Chen and P. E. Reyes-Morel, "Transformation Plasticity and Transformation Toughening in Mg-PSZ and Ce-PSZ"; pp. 75–89 in Materials Research Society Symposium Proceedings, Vol. 78. Edited by P. F. Becher, M. V. Swain, and S. Sōmiya. Materials Research Society, Pittsburgh, PA, 1987.

[16]D. B. Marshall, "Strength Characteristics of Transformation-Toughened Zirconia," *J. Am. Ceram. Soc.*, 69 [3] 173–80 (1986).

[17]M. J. Readey, A. J. Heuer, and R. W. Steinbrech, "Crack Propagation in Mg-PSZ"; pp. 107–20 in Materials Research Society Symposium Proceedings, Vol. 78. Edited by P. F. Becher, M. V. Swain, and S. Sōmiya. Materials Research Society, Pittsburgh, PA, 1987.

[18]D. B. Marshall and M. V. Swain, "Crack Resistance Curves in Magnesia-Partially-Stabilized Zirconia," *J. Am. Ceram. Soc.*, 71 [6] 399–407 (1988).

[19]D. R. Clarke and F. Adar, "Measurement of the Crystallographically Transformed Zone Produced by Fracture in Ceramics Containing Tetragonal Zirconia," *J. Am. Ceram. Soc.*, 65 [6] 284–88 (1982).

[20]D. R. Clarke and F. Adar, "Raman Microprobe Spectroscopy of Polyphase Ceramics"; pp. 199–214 in Advances in Materials Characterization. Edited by D. R. Rossington, R. A. Condrate, and R. L. Snyder. Plenum, New York, 1983.

[21]L. Soto and F. Adar, "Raman Microprobe Characterization of ZrO_2 Inclusions in Glass Lightguides"; pp. 121–24 in Microbeam Analysis. Edited by A. D. Romig, Jr., and J. I. Goldstein. San Francisco Press, San Francisco, CA, 1984.

[22]P. F. Becher, "Toughening Behavior in Ceramics Associated with the Transformation of Tetragonal ZrO_2," *Acta Metall.*, 34 [10] 1885–91 (1986).

[23]V. G. Keramidas and W. B. White, "Raman Scattering Study of the Crystallization and Phase Transformation of ZrO_2," *J. Am. Ceram. Soc.*, 57 [1] 22–24 (1974).

[24]M. Ishigame and T. Sakurai, "Temperature Dependence of the Raman Spectra of ZrO_2," *J. Am. Ceram. Soc.*, 60 [7–8] 367–69 (1977).

[25]C. H. Perry, D.-W. Liu, and R. P. Ingel, "Phase Characterization of Partially Stabilized Zirconia by Raman Spectroscopy," *J. Am. Ceram. Soc.*, 68 [8] C-184–C-187 (1985).

[26]D. K. Veirs, V. F. K. Chia, and G. M. Rosenblatt, "Raman Spectroscopy Applications of an Imaging Photomultiplier Tube," *Appl. Opt.*, 26 [17] 3530–35 (1987).

[27]R. H. J. Hannink and M. V. Swain, "Magnesia-Partially-Stabilized Zirconia: The Influence of Heat Treament on Thermomechanical Properties," *J. Aust. Ceram. Soc.*, 18, 53–62 (1982).

[28]D. B. Marshall and M. R. James, "Reversible Stress-Induced Martensitic Transformation in ZrO_2," *J. Am. Ceram. Soc.*, 69 [3] 215–17 (1986).

[29]R. H. Dauskardt, W. Yu, and R. O. Ritchie, "Fatigue Crack Propagation in Transformation-Toughened Ceramic," *J. Am. Ceram. Soc.*, 70 [10] C-248–C-252 (1987).

[30]M. Delhaye and P. Dhamelincourt, "Raman Microprobe and Microscope with Lazer Excitation," *J. Raman Spectrosc.*, 3 [1] 33–34 (1975).

[31]P. Dhamelincourt, "Developments and Applications of the Mole Laser Raman Microprobe"; pp. 155–64 in Microbeam Analysis— 1979. Edited by D. E. Newbury. San Francisco Press, San Francisco, CA, 1979.

[32]E. S. Etz, "Raman Microprobe Analysis, Principles and Applications"; pp. 67–82 in Scanning Electron Microscopy— 1979. Edited by Om Johari. IIT Research Institute, Chicago, 1979.

[33]D. B. Marshall, Rockwell International Science Center, Thousand Oaks, CA; private communication, 1987.

[34]R. H. Dauskardt, D. B. Marshall, and R. O. Ritchie, "Mechanisms of Fatigue-Crack Propagation in Transformation-Toughened MgO-Partially-Stabilized Zirconia"; to be published in Fracture Mechanics/Structural Ceramics, Materials Research Society International Meeting on Advanced Materials, Ikebukuro, Tokyo, Japan, June 1988. Materials Research Society, Pittsburgh, PA, 1989.   □

journal

Production of Fine Ceramic Powders from Chloromethylsilanes Using Pulsed Excimer Radiation

J. A. O'Neill, M. Horsburgh, J. Tann, K. J. Grant, and G. L. Paul

Centre for Industrial Laser Applications, University of New South Wales, Kensington, New South Wales 2033, Australia

W. Sinclair

BHP Melbourne Research Laboratories, Mulgrave, Victoria 3170, Australia

Ceramic powders have been produced by the photodecomposition of chloromethylsilanes using a pulsed excimer laser operating at 193 nm. These feedstocks are cheaper and easier to handle than SiH_4, the main feedstock used in earlier work using continuous-wave CO_2 lasers as the irradiation source.

Powders were produced from photolysis of silanes containing methyl groups without the addition of any coreagents, while the two silanes tested containing only chlorine and hydrogen ligands, $SiCl_3H$ and $SiCl_4$, required the addition of H_2 as a coreagent for significant yields of powder to be produced. The powders produced were found to be low in chlorine, with amorphous Si powders or β-SiC being produced depending on feedstock. Particle sizes measured from electron micrographs varied from less than 10 nm to 1.5 μm. [Key words: silanes, powders, lasers, chlorine, photodecomposition.]